

# pH-Responsive Gas–Water–Solid Interface for Multiphase Catalysis

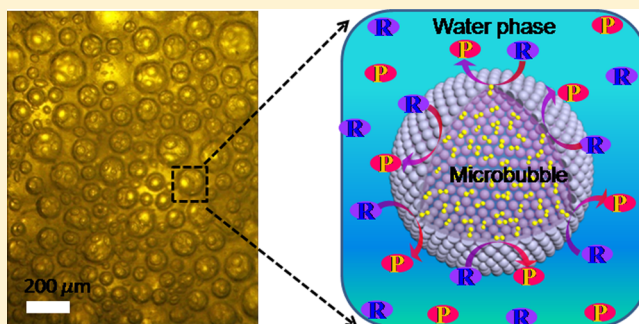
Jianping Huang,<sup>†</sup> Fangqin Cheng,<sup>‡</sup> Bernard P. Binks,<sup>§</sup> and Hengquan Yang<sup>\*,†</sup>

<sup>†</sup>School of Chemistry and Chemical Engineering and <sup>‡</sup>Institute of Resources and Environment Engineering, Shanxi University, Wucheng Road 92, Taiyuan 030006, China

<sup>§</sup>Surfactant & Colloid Group, Department of Chemistry, University of Hull, Hull HU6 7RX, United Kingdom

**S** Supporting Information

**ABSTRACT:** Despite their wide utility in laboratory synthesis and industrial fabrication, gas–water–solid multiphase catalysis reactions often suffer from low reaction efficiency because of the low solubility of gases in water. Using a surface-modification protocol, interface-active silica nanoparticles were synthesized. Such nanoparticles can assemble at the gas–water interface, stabilizing micrometer-sized gas bubbles in water, and disassemble by tuning of the aqueous phase pH. The ability to stabilize gas microbubbles can be finely tuned through variation of the surface-modification protocol. As proof of this concept, Pd and Au were deposited on these silica nanoparticles, leading to interface-active catalysts for aqueous hydrogenation and oxidation, respectively. With such catalysts, conventional gas–water–solid multiphase reactions can be transformed to H<sub>2</sub> or O<sub>2</sub> microbubble reaction systems. The resultant microbubble reaction systems exhibit significant catalysis efficiency enhancement effects compared with conventional multiphase reactions. The significant improvement is attributed to the pronounced increase in reaction interface area that allows for the direct contact of gas, water, and solid phases. At the end of reaction, the microbubbles can be removed from the reaction systems through changing the pH, allowing product separation and catalyst recycling. Interestingly, the alcohol oxidation activation energy for the microbubble systems is much lower than that for the conventional multiphase reaction, also indicating that the developed microbubble system may be a valuable platform to design innovative multiphase catalysis reactions.



conventional gas–water–solid multiphase reactions can be transformed to H<sub>2</sub> or O<sub>2</sub> microbubble reaction systems. The resultant microbubble reaction systems exhibit significant catalysis efficiency enhancement effects compared with conventional multiphase reactions. The significant improvement is attributed to the pronounced increase in reaction interface area that allows for the direct contact of gas, water, and solid phases. At the end of reaction, the microbubbles can be removed from the reaction systems through changing the pH, allowing product separation and catalyst recycling. Interestingly, the alcohol oxidation activation energy for the microbubble systems is much lower than that for the conventional multiphase reaction, also indicating that the developed microbubble system may be a valuable platform to design innovative multiphase catalysis reactions.

## 1. INTRODUCTION

Solid catalyst-containing gas–water multiphase reactions are widely used in laboratory synthesis and industrial fabrication of various fine chemicals via hydrogenation, oxidation, hydroformylation, and biochemical processes.<sup>1–6</sup> Because of the extremely low solubility of gases in water, e.g., H<sub>2</sub> and O<sub>2</sub>, the catalytic efficiency of these multiphase reactions is usually significantly suppressed.<sup>7–9</sup> To address this limitation, many methods have been developed as follows. Introducing a cosolvent or raising the gas pressure is employed to increase the gas molecule concentrations in liquids.<sup>1,10,11</sup> Organic solvents may be added to form water-in-oil Pickering emulsions, in which the continuous oil phase can increase gas molecule concentrations in the whole systems and the larger oil–water interface benefits the reaction.<sup>3,9,12</sup> Obviously, these methods require extra additives or impact process safety and do not enable gas–water–solid phases to contact directly. Alternatively, engineering strategies such as bubbling fluidized beds, packed bubble columns, “tube-in-tube” techniques, and microbubble generators have been exploited to increase the gas–liquid interface area.<sup>13–20</sup> The work of the Mase group on bare micro- or nanobubbles is particularly noteworthy,<sup>7,18,19</sup> although little mention is made of their sizes. These methods are more environmentally acceptable because of the avoidance of organic solvents. However, these strategies require specific

equipment and often lead to incomplete utilization of the gas because of the buoyancy of large bubbles and their rapid collapse. Moreover, they do not guarantee that the solid catalyst will locate at the gas–liquid interfaces. Accordingly, developing a simple, effective method to create direct contact at the gas–water–solid interface is still a much-sought-after goal.<sup>14</sup>

In parallel, natural systems can efficiently deal with multiphase processes such as photosynthesis and respiration.<sup>21</sup> One key feature of the natural systems is the unique air–aqueous interface that allows gas-phase O<sub>2</sub> and CO<sub>2</sub> to expeditiously enter aqueous media, which may constitute an important feature for future non-natural multiphase systems. More interestingly, various surface characterization techniques and theoretical calculations point out that the gas–water interface has unique properties that are not possessed by the bulk aqueous solution. For example, OH<sup>−</sup> or H<sup>+</sup> may be preferentially adsorbed in the interfacial region although there is considerable disagreement on which one has this interfacial propensity.<sup>22–26</sup> It is also revealed that some organic molecules at the gas–water interface have certain orientations.<sup>27</sup> Also, at the gas–water interface, gaseous molecules are more easily bound with metal complexes in solution.<sup>28</sup> These unique

Received: September 17, 2015

Published: November 2, 2015

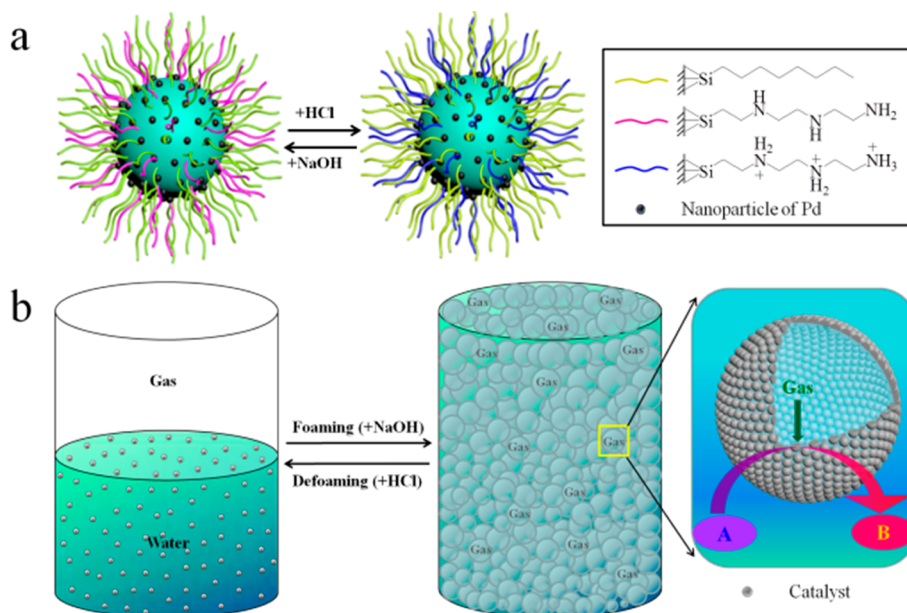


**Figure 1.** Proposed solid catalyst particle-stabilized microbubble strategy. (a) Structure of a pH-responsive, partially hydrophobic nanoparticle catalyst and the process of protonation and deprotonation with acid or base. (b) Schematic illustration for transforming a gas–water–solid multiphase reaction to a catalyst particle-stabilized microbubble system and destruction of the latter at the end of reaction. A represents a reactant molecule, and B represents a product molecule.

interface properties probably affect the catalysis process and outcomes but are rarely explored. One of the main reasons lies in the difficulty in obtaining a sufficiently large, stable, and controllable gas–water interface.

It has been found that partially hydrophobic nanoparticles can assemble at the gas–water interface, thus stabilizing gas bubbles in water.<sup>29–42</sup> In such a scenario, gas, water, and solid phases can directly contact each other.<sup>43</sup> However, bubbles themselves are not always desirable in practice because of the problems arising in the subsequent product and catalyst separation. Although alcohols or silicone oils can be used to destroy bubbles,<sup>44–47</sup> the defoamer separation requires extra procedures. It is envisioned that if the bubble sizes can be decreased to the micrometer level and at the same time bubbling can be switched in a controllable way then solid-particle-stabilized microbubbles might be exploited to construct efficient multiphase catalysis systems and address the interface catalysis effects.

Herein, we demonstrate a novel strategy to construct efficient gas–water–solid multiphase reactions by creating smart, particle-stabilized microbubbles. This strategy uses a pH-responsive nanoparticle catalyst, in which the surface wettability can be switched between partially hydrophobic and hydrophilic by addition of acid or base, as illustrated in Figure 1a. Such a switch can drive the system between a stable microbubble system and a conventional (bubble-free) one. At the beginning of reaction, a conventional gas–liquid–solid multiphase catalysis reaction can be transformed to a microbubble system (Figure 1b). Because of the assembly of catalyst particles at the gas–water interface, gas, liquid, and solid phases are in direct contact simultaneously. As a consequence, the catalytic efficiency is expected to be significantly enhanced. At the end of reaction, the microbubble system is destroyed by adding a small amount of acid, allowing product and catalyst separation. After the recovered nanoparticle catalyst is treated with base, the microbubble system can be obtained again in the next reaction cycle. Such a microbubble system is expected not only

to access more efficient multiphase reactions but also to be of use in manifesting gas–liquid–solid interface catalysis effects.

## 2. RESULTS AND DISCUSSION

### 2.1. Preparation and Characterization of Interfacially Active Nanoparticles.

To construct the proposed reaction system, we first need to create a pH-responsive, partially hydrophobic nanoparticle catalyst. Although a pH-responsive latex for the formation of foams has been reported, bubbling with these polymer particles requires the addition of salt,<sup>48</sup> which is not desired for catalytic reactions. Moreover, for catalytic applications, inorganic materials are preferred because of their robustness. Silica is a good choice because it is widely used as commercial catalyst support. A mixture of hydrophobic,  $(\text{MeO})_3\text{Si}(\text{CH}_2)_7\text{CH}_3$ , and relatively hydrophilic,  $(\text{MeO})_3\text{SiCH}_2\text{CH}_2\text{CH}_2(\text{NHCH}_2\text{CH}_2)_2\text{NH}_2$ , organosilane modifiers was used to modify silica nanoparticles because this protocol has proven effective at tuning the surface hydrophobicity/hydrophilicity balance for forming Pickering emulsions in our recent work.<sup>49</sup> Herein, as an extension to this protocol, we used smaller silica nanoparticles (SN, ca. 50–70 nm in diameter) because the detachment of smaller particles from a gas–water interface is energetically easier.<sup>50</sup> Moreover, the triamine group concentration on the silica surface was significantly increased to obtain a more hydrophilic surface. The mole fraction of the triamine organosilane in the total silylating reagent mixture was varied from 5 to 25% (octyl organosilane from 95 to 75%), and the total amount of organosilanes was kept constant. The resultant bifunctionalized silica nanoparticles are named as SN-ON( $x$ ), where  $x = 5, 10, 15, 20,$  or  $25$ . (O refers to octyl organosilane, N refers to triamine organosilane, and  $x$  refers to the mole fraction of triamine organosilane.) For comparison, we also prepared octyl- and triamine-monofunctionalized silica particles, denoted as SN-O and SN-N, respectively.

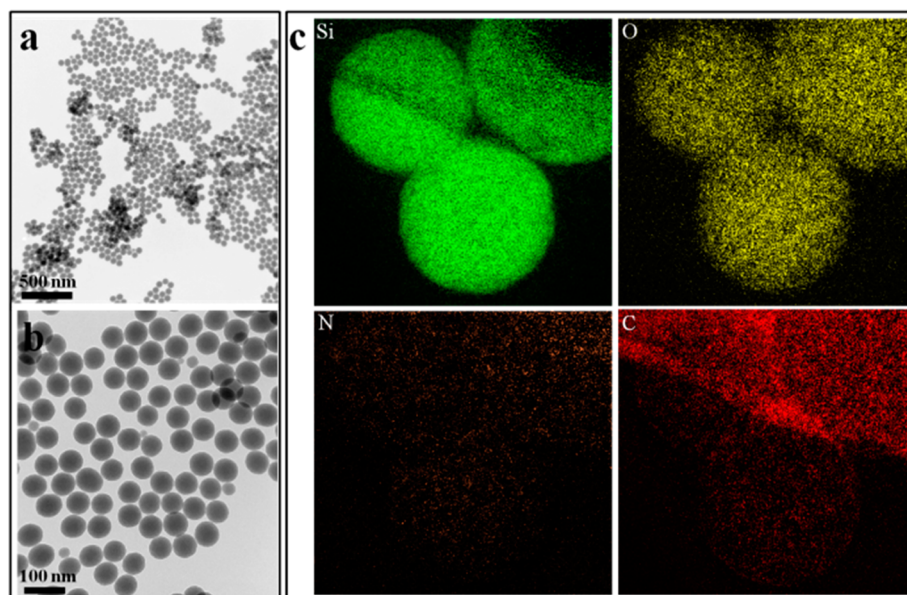


**Figure 2.** Characterization of the SN-ON(15) nanoparticles. (a) TEM image, scale bar = 500 nm. (b) TEM image, scale bar = 100 nm. (c) Element mapping with electron energy-loss spectroscopy (EELS).

The morphology and composition of the modified particles were characterized with transmission electron microscopy (TEM),  $N_2$  sorption, solid-state NMR, X-ray photoelectron spectroscopy (XPS), element mapping, and elemental analysis. For example, SN-ON(15) consists of uniform monodisperse spheres with diameters around 50–70 nm (Figures 2a,b). It is almost nonporous because its specific surface area is only  $50 \text{ m}^2 \text{ g}^{-1}$  (Figure S1). The XPS results indicate that octyl and triamine groups are both grafted on the silica surface because C and N elements are both found simultaneously (Figure S2). The solid-state  $^{13}\text{C}$  CP-MAS NMR spectrum exhibits C signals, which can be assigned to these two groups (Figure 3a). In the solid-state  $^{29}\text{Si}$  CP-MAS NMR spectrum (Figure 3b),  $T^3$  [ $\text{SiR}(\text{OSi})_3$ ] and  $T^2$  [ $\text{SiR}(\text{OSi})_2(\text{OH})$ ] bands appear, indicating that these two functionalities are linked to the silica surface through Si–O–Si bonds. In the electron energy-loss spectrum (EELS) for the elemental mapping (Figure 2c), C and N elements were found to be uniformly distributed on silica nanospheres, indicating that these two functionalities are both uniformly distributed on the silica nanospheres. Elemental analysis gives quantitative results of functionality loadings (Figure 3c and Table S1). The total concentration of these two functionalities is up to ca.  $0.5 \text{ mmol g}^{-1}$ , indicating a high level of functionalization. Notably, for the bifunctionalized silica nanoparticles, the molar ratio of hydrophilic triamine to hydrophobic octyl chains gradually increases from 0.19 to 0.86 (Figure 3c), underlining that the surface chemistry can be finely tuned by varying the mole fraction of these two organosilanes during particle surface modification.

**2.2. Nanoparticle-Stabilized Microbubbles.** The ability of these nanoparticles to stabilize microbubbles (i.e., foamability) was next assessed. After stirring a mixture of nanoparticles and water in air for 10 min at 1200 rpm (with a magnetic stirrer bar), different phenomena were observed. As shown in Figure 4a, the raw unfunctionalized silica particles and SN-N particles remain dispersed in water forming a milky-white suspension, whereas SN-O particles float on the water surface. These three particle types do not lead to particle-stabilized bubbles. In contrast, for the bifunctionalized particles, a large

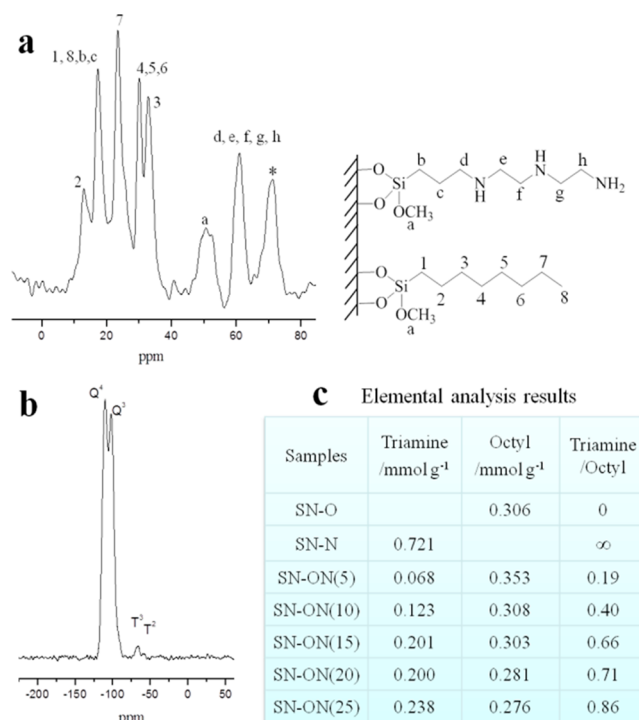


**Figure 3.** Characterization of SN-ON(15) nanoparticles. (a) Solid-state  $^{13}\text{C}$  CP-MAS NMR spectrum, in which the peak marked \* may be attributed to the buried  $-(\text{CH}_2\text{CH}_2\text{O})_n$  groups inside the silica sphere during synthesis. (b) Solid-state  $^{29}\text{Si}$  CP-MAS NMR spectrum. (c) Grafted amounts of triamine and octyl groups on functionalized silica. Triamine/octyl is the molar ratio based on results of elemental analysis.

amount of micrometer-sized air bubbles are observed within water even in the absence of salt. The foamability, defined as the volume ratio of foam to that of initially used water ( $V_{\text{foam}}/V_{\text{water}}$ ; see legend of Figure 4), is remarkably different; however, judged from the foam height, Figure 4b displays the foamability of these samples versus the molar ratio of triamine/octyl groups

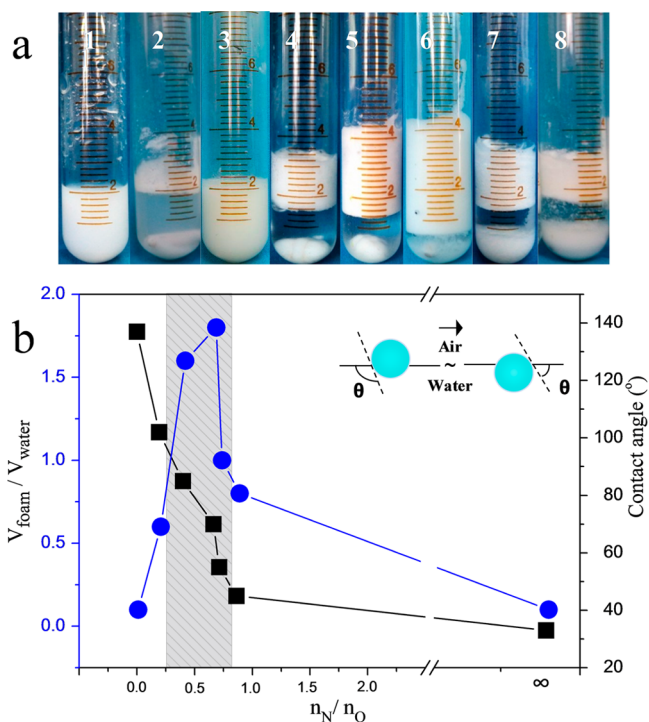


**Figure 4.** Bubbling ability of the silica nanoparticles. (a) Appearance of a mixture of 0.15 g of nanoparticles and 2 mL of water after stirring in air and further standing for 1 h. 1, unfunctionalized silica; 2, SN-O; 3, SN-N; 4, SN-ON(5); 5, SN-ON(10); 6, SN-ON(15); 7, SN-ON(20); 8, SN-ON(25). (b) Bubbling ability (foamability, blue points) and three-phase contact angle (black points) versus the molar ratio of triamine groups to octyl groups,  $n_N/n_O$ .  $V_{\text{foam}}/V_{\text{water}}$  = foam volume/initial water volume.  $V_{\text{foam}}$  is defined as the volume between the foam/water boundary and foam/air boundary.

on the particle surfaces. Interestingly, the foamability first increases and then decreases as the value of  $n_N/n_O$  increases, and the average size of the bubbles correspondingly first decreases and then increases (Figure S3). This is similar to what was observed for modified fumed-silica-stabilized foams.<sup>32</sup> In the case of SN-ON(15) particles ( $n_N/n_O = 0.66$ ), the foamability reaches its maximum value (1.8), and the bubble sizes are a minimum value (centered around 80–100  $\mu\text{m}$ ) and uniformly distributed in the system. These findings indicate that our protocol allows the silica nanoparticle to stabilize microbubbles in water, and its ability can be finely tuned by varying the molar ratio of the modifiers.

The results of the contact angle measurement of a water drop in air on disks composed of powdered particles provide an explanation for the differences in foamability. The contact angles measured through water on the substrates of SN-O, SN-ON(5), SN-ON(10), SN-ON(15), SN-ON(20), SN-ON(25), and SN-N samples decrease progressively from 137 to 102, 85, 70, 55, 45, and 33° (Figures 4b and S4). SN-O is too hydrophobic to stabilize foams, and SN-N is too hydrophilic. Only particles exhibiting partial hydrophobicity can stabilize air-in-water foams.<sup>32</sup> Moreover, after standing for 5 days, the microbubbles stabilized with SN-ON(10), SN-ON(15), and SN-ON(20) particles show no apparent change in terms of their appearance and bubble sizes, indicating that they have high stability against bubble coalescence, disproportionation, and water drainage (Figure S5).

### 2.3. pH-Triggered Switch between Microbubble and Bubble-Free Systems.

As expected, these microbubbles are pH-responsive because acid addition protonates the amine groups on the silica surfaces, thus increasing their hydrophilicity (Figure 1a). As Figure 5a shows, the microbubbles stabilized with the SN-ON(15) particles undergo complete destruction, becoming a suspension after the pH is reduced to 3–4 with HCl. The process of collapse of the microbubbles was accomplished within 3–6 min through gentle stirring. Moreover, this suspension is restored to a microbubble system after adjusting the pH back to 7–8 with stirring. Such a pH-triggered switch can be reversibly repeated at least 10 times. The foamability exhibits no significant change in each cycle. Optical micrographs further confirm these results (Figure 5b). In the first cycle, bubbles of diameter between 40 and 200  $\mu\text{m}$  are observed. After lowering the pH, these microbubbles disappear. It is the same scenario with the 10th cycle.

Such a pH-responsive behavior is supported by the results of zeta potential and three-phase contact angle measurements. As shown in Figure 5c, at pH 3 the zeta potential of SN-ON(15) particles is +31.7 mV, indicating that the triamine on the silica surface is protonated. As the pH increases, the zeta potential gradually decreases because of deprotonation. When the pH reaches 6, the zeta potential is close to zero, suggesting nearly complete deprotonation of the protonated triamines. In contrast, for the bare silica nanoparticles (SN), the zeta potential is ca. 0 mV at pH 3, and becomes –23 mV at pH 6 because of deprotonation of surface silanol groups (SiOH). The difference between these two samples is attributed to the surface modification that alters the surface chemical properties of silica. The protonation of the amine groups results in the particle surface becoming more hydrophilic, whereas the deprotonation of protonated amines on the silica surface renders the particle surface partially hydrophobic. The air–water–solid three-phase contact angle for SN-ON(15) substrates (without any treatment) was measured as 70° (Figure 5d), which decreased to 44° after treatment with HCl solution and was restored to 73° after subsequent treatment with NaOH solution. These changes in the surface wettability of the particles are the origin of the switching between microbubble and bubble-free aqueous dispersions.<sup>51</sup>

**2.4. Catalytic Application I: Hydrogenation.** We then selected a reaction of hydrogenation to assess the microbubble system because hydrogenation of unsaturated groups is one of the most important platforms for the synthesis of various fine chemicals.<sup>52–54</sup> Because of the good complexation ability of triamine, it is easy to load Pd nanoparticles onto the SN-ON( $x$ ) particles via the adsorption of Pd(OAc)<sub>2</sub> followed by reduction with NaBH<sub>4</sub>. The resultant hydrogenation catalyst is named as Pd/SN-ON( $x$ ), with the Pd loading being kept at 0.25 wt %. As the TEM image shows (Figure 6a), Pd nanoparticles with a size of ca. 1 nm are homogeneously distributed on the silica surface. The small size and uniform size distribution should be attributed to the presence of triamine groups that can prevent Pd nanoparticles from growing into large particles through coordination. The energy-dispersive X-ray spectrum (EDX) confirms the presence of Pd, N, C, O, and Si elements on the catalyst.

The hydrogenation of a water-soluble reactant, *p*-nitrophenol, was used to evaluate the catalysis efficiency (CE) of this set of Pd/SN-ON( $x$ ) catalysts. To obtain a microbubble reaction system, we blended the Pd/SN-ON( $x$ ) particles with the SN-ON( $x$ ) particles to increase the total nanoparticle

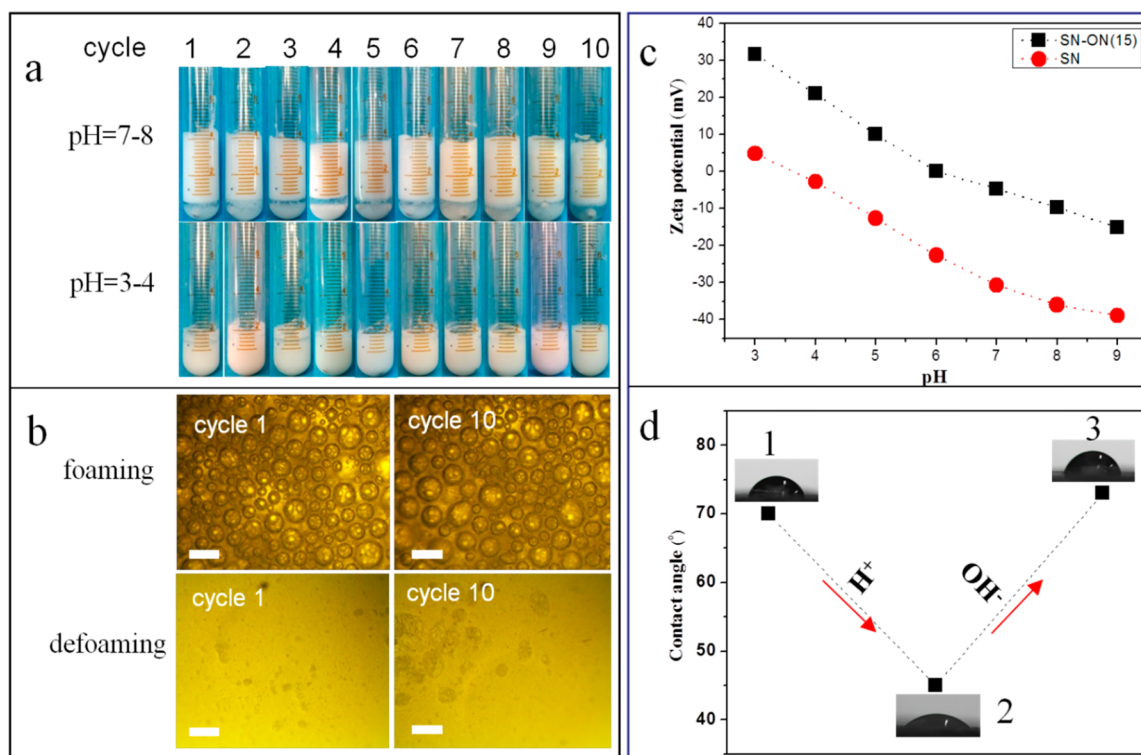


**Figure 5.** pH-triggered switch between microbubble and bubble-free systems using 7.5 wt % SN-ON(15) particles. (a) Appearance of systems in 10 switch cycles in response to pH. HCl solution (1 M) and NaOH solution (1 M) were used to adjust the pH. (b) Optical micrographs for the 1st and the 10th cycles; scale bar = 200  $\mu\text{m}$ . (c) Zeta potentials of SN-ON(15) particles and SN particles in water as a function of pH. (d) Photos and contact angles of water drops in air on disks of SN-ON(15) particles treated under different conditions: (1) Fresh SN-ON(15) particles (without acid/base treatment), (2) SN-ON(15) particles after treatment with HCl solution (0.5 mM) and then compressed to a disk, and (3) protonated SN-ON(15) particles treated with NaOH solution (0.5 mM) and then compressed to a disk.

concentration. (The mass ratio of Pd/SN-ON( $x$ ) to SN-ON( $x$ ) is kept at 1:3; SN-ON( $x$ ) proved catalytically inactive for hydrogenation.) The molar ratio of substrate to Pd catalyst ( $S/C$ ) for hydrogenations was kept at the same level. The batch reactions were carried out in an autoclave at a pressure of 0.9 MPa. Interestingly, it was found that the set of catalysts gave remarkably different conversions under the same conditions (Table S2). On the basis of the conversions, one can calculate the CE (defined in the legend of Figure 7).

The CE values for these reaction systems is remarkably dependent on the value of  $x$  (the molar fraction of triamine), as shown in Figure 7a. The CE first increases and then begins to decrease as  $n_N/n_O$  increases, namely, following the order of Pd/SN-ON(5) < Pd/SN-ON(10) < Pd/SN-ON(15) > Pd/SN-ON(20) > Pd/SN-ON(25) > Pd/SN-N. Interestingly, this maximum in CE goes alongside that of the foamability (Figure 4b). Among these systems, the microbubble system stabilized by the Pd/SN-ON(15) particles has the highest CE, which is nine times higher than that of the microbubble-free system using Pd/SN-N particles. The appearance of these two systems is shown in Figure S6 where one can see  $\text{H}_2$  microbubbles in the former system. In contrast, this set of Pd/SN-ON( $x$ ) catalysts give similar conversions in bulk methanol, indicating that their intrinsic activity is around the same (Table S3).

These differences between the microbubble systems and conventional gas–water–solid multiphase reactions imply that the enhanced CE may be related to the presence of a large number of micrometer-sized bubbles in the former that create a large reaction interface area and allow gas, reactant, and catalyst to keep direct contact. To further confirm this, we conducted

another set of experiments in which a fixed amount of the Pd/SN-ON(15) particles was blended with gradually increased amounts of the catalytically inactive SN-ON(15) particles. (The ratio was increased from 1:0 to 1:1, 1:2, 1:3.) As Figure 7b shows, the CE dramatically increases upon increasing the amount of the catalytically inactive SN-ON(15) particles despite using the same amount of catalytically active Pd/SN-ON(15). The CE for a mixture of Pd/SN-ON(15) and SN-ON(15) particles (1:3) is 5.1 times higher than that of pure Pd/SN-ON(15) (1440 vs 282  $\text{mol mol}^{-1} \text{h}^{-1}$ ). Notably, in the conventional bulk three-phase system using 16 vol % isopropyl alcohol as cosolvent in water, the CE of this set of mixture of Pd/SN-ON(15) and SN-ON(15) particles does not change appreciably upon varying the mass ratio of Pd/SN-ON(15) to SN-ON(15), as shown in Figure S7. Meanwhile, as the amount of SN-ON(15) particles increases, the foamability ( $V_{\text{foam}}/V_{\text{water}}$ ) increases (Figures 7b and S8). It is clearly evident that the increase in CE mirrors that of the increase in foamability, confirming that the CE enhancement is due to the formation of stable microbubbles that increase the reaction interface area of gas–water–solid.

To further confirm CE enhancement effects employing the microbubble systems, we compared the CE of the microbubble systems and that of the conventional bulk gas–water–solid multiphase systems using more substrates. Because of the presence of a given amount of isopropyl alcohol, the conventional three-phase reaction systems are microbubble-free. The results of the hydrogenation of four water-soluble substrates in these two systems are summarized in Table 1. The microbubble system gave a full conversion of *p*-nitrophenol,

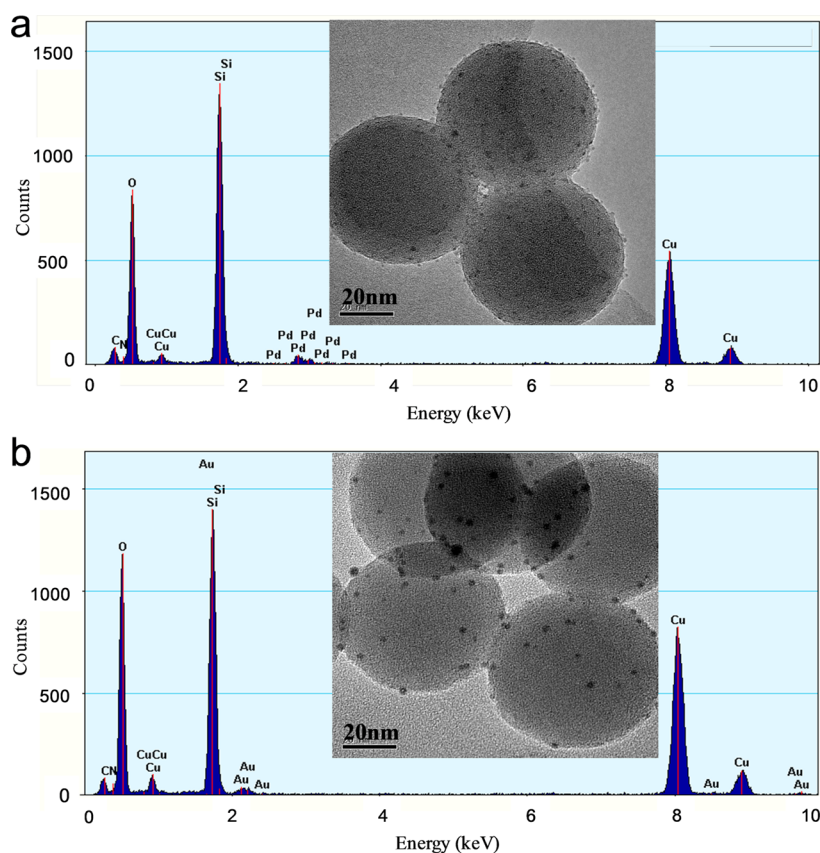


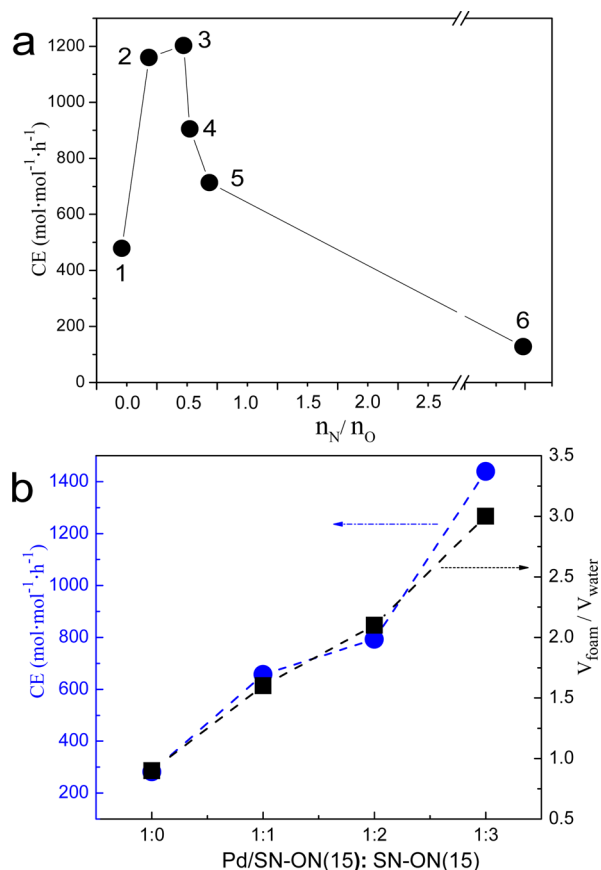
**Figure 6.** TEM images and EDX spectra of catalysts. (a) Pd/SN-ON(15) catalyst. (b) Au/SN-ON(15) catalyst.

whereas the conventional three-phase reaction system afforded a conversion of only 19% under the same conditions, i.e., a 5.3-fold conversion enhancement was obtained. At low  $H_2$  pressure (0.1 MPa), a microbubble hydrogenation system can also be obtained although a longer reaction time is required for 100% conversion. The microbubble system also gives a much higher conversion than the conventional system in this case. Such a remarkable contrast was also found with other substrates such as *o*-nitrophenol, allyl alcohol, and *cis*-2-butene-1,4-diol. These results further demonstrate the versatility and high efficiency of the catalyst-particle-stabilized microbubble strategy. As expected, the microbubble hydrogenation systems can be easily switched through adjusting the pH to enable the recycling of the solid catalyst. As shown in Figure S9, after five reaction cycles the microbubble system is still obtained, and the CE is still relatively high. The slight decrease in catalyst efficiency is mainly due to the aggregation of Pd nanoparticles (Figure S10) because the bubbling ability and the Pd loading have no appreciable change.

**2.5. Catalytic Application II: Oxidation.** Our strategy can be extended to other types of gas–water–solid multiphase reactions, e.g., alcohol oxidation with  $O_2$ .<sup>4,55–58</sup> Au nanoparticles were deposited on the SN-ON(15) particle surface through acid–base interaction with  $HAuCl_4$  followed by reduction with  $NaBH_4$ , leading to a Au/SN-ON(15) catalyst. The Au loading is 0.8 wt %. The TEM image (Figure 6b) shows that Au particles with a size of ca. 2–4 nm are uniformly distributed on the silica surface. The EDX spectrum further confirms that Au, N, C, O, and Si elements were all present on the catalyst as expected (Figure 6b).

Oxidation was carried out in an autoclave under an  $O_2$  pressure of 0.2 MPa (900 rpm). In the presence of a mixture of the Au/SN-ON(15) catalyst particles and the SN-ON(15) particles (the mass ratio of the former to latter is 2:3), a microbubble system was observed in the oxidation of 2-hydroxybenzyl alcohol to salicyl aldehyde (Figures 8 and S11). The microbubble oxidation system afforded a conversion of 93% within 5 h, whereas the conventional multiphase system gave a conversion of only 45%. As expected, the microbubbles in the reaction system can be destroyed in a controllable fashion at the end of reaction (Figures 8 and S11). When the pH of the reaction system was adjusted to 3–4 at the end of reaction, the microbubble system changed to a conventional bubble-free suspension under gentle stirring.



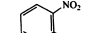
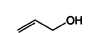

The catalyst could be isolated from the reaction system via centrifugation. After being treated with a small amount of base, the recovered catalyst was directly used in the next batch reaction. A microbubble system was formed again (Figure S11). In the second reaction cycle, 76% conversion of 2-hydroxybenzyl alcohol was achieved (Figure 8c). From the third to the ninth reaction cycle, microbubble systems could be still formed, and conversions of between 73 and 93% were obtained. In the 10th reaction cycle, the bubble sizes had no significant change in comparison with those of the first reaction cycle (Figure 8b), and the conversion of 2-hydroxybenzyl alcohol was more than 70% within a slightly prolonged reaction time (legend of Figure 8). The loss of reaction efficiency may be mainly due to the growth of Au nanoparticles because their ability to stabilize  $O_2$  microbubbles and the Au loading have no appreciable change (Figures 8b and S10).



**Figure 7.** Results of *p*-nitrophenol hydrogenation in different reaction systems. (a) Catalysis efficiency (CE) of the microbubble systems with [Pd/SN-ON(*x*) + SN-ON(*x*)] or [Pd/SN-N + SN-N] versus the ratio  $n_N/n_O$ . The mass ratio of Pd catalyst to SN support is 1:3. 1,  $x = 5$ ; 2,  $x = 10$ ; 3,  $x = 15$ ; 4,  $x = 20$ ; 5,  $x = 25$ ; and 6, Pd/SN-N + SN-N. CE = moles of converted substrate/mol of Pd  $\times$  reaction time (h). Reaction conditions: 2.5 mL of water, 1.32 mmol *p*-nitrophenol, 0.0469 g of Pd/SN-ON(*x*) or Pd/SN-N, 0.1409 g of SN-ON(*x*) or SN-N, 0.9 MPa, 25 °C, 1200 rpm, 1 h. (b) Variation of CE (blue points) and foamability (black points) versus the mass ratio of Pd/SN-ON(15) to SN-ON(15). Reaction conditions: Pd/SN-ON(15) amount was fixed at 0.0469 g, and the SN-ON(15) amount was varied. The mass ratio of Pd/SN-ON(15):SN-ON(15) was changed from 1:0 to 1:1, 1:2, and 1:3. Other conditions are the same as in a except 50 min of reaction time.

Moreover, for other different substrates including *m*-hydroxybenzyl alcohol, *p*-hydroxybenzyl alcohol, 3,5-dihydroxybenzyl alcohol, O<sub>2</sub> microbubble systems could also be obtained. The reaction results are summarized in Table 2. For all the investigated substrates, the microbubble systems also gave much higher conversions than the conventional gas–liquid–solid multiphase systems, further highlighting the reaction efficiency enhancement of microbubble systems. It is well-recognized that alcohol oxidation with O<sub>2</sub> is a relatively slow reaction, which is supported by our above experiments in which it took several hours to complete the oxidation reaction even with the low molar ratios of substrate/Au (50:1). This means that under the investigated reaction conditions (900 rpm), the reaction rate enhancement is not due to increasing mass transport by the particle-stabilized microbubbles. This claim is further supported by our experiments in that the reaction rate of both the conventional multiphase system and

**Table 1.** Comparison of Hydrogenation in the Microbubble Systems and in the Conventional Bulk Gas–Liquid–Solid Multiphase Systems<sup>a</sup>

Reactant	Solid <sup>b</sup> /wt.%	S/C <sup>c</sup>	Temp. <sup>d</sup> /°C	P <sup>e</sup> /MPa	t <sup>f</sup> /h	Conv. <sup>g</sup> /%
	7.5	800	25	0.9	0.67	100 (19)
	7.5	800	25	0.1	2	100 (12)
	4.5	1500	50	0.9	1	91 (25)
	7.5	2500	25	0.1	0.33	91 (22)
	4.5	4000	25	0.3	0.67	96 (35)

<sup>a</sup>The reaction conditions for foam systems: 2.5 mL of water, and 1200 rpm. The reaction conditions for the conventional three-phase systems are: a mixture of 0.4 mL of isopropyl alcohol and 2.1 mL of water as solvent, 1200 rpm. <sup>b</sup>The total mass fraction of catalyst and SN-ON(15) particles with respect to solvent. <sup>c</sup>The molar ratio of substrate (S) to Pd catalyst (C). <sup>d</sup>Reaction temperature. <sup>e</sup>H<sub>2</sub> pressure. <sup>f</sup>Reaction time. <sup>g</sup>Conversions determined by GC; the data in parentheses are the conversions obtained in conventional three-phase systems.

the microbubble systems no longer increased when the stirring speed was increased up to 800 rpm (Table S4).

To clarify the difference in CE, we monitored the kinetics of the microbubble system and the conventional multiphase system. It was found that these two systems displayed pseudo-first-order kinetics with respect to 2-hydroxybenzyl alcohol (Figure S12; in these systems O<sub>2</sub> is in great excess), which is in good agreement with previous work.<sup>55</sup> On the basis of these kinetic plots at different temperatures, the estimated activation energy ( $E_a$ ) of the conventional reaction system is  $58.6 \pm 2.4$  kJ/mol, whereas that of the microbubble reaction system is  $40.7 \pm 3.1$  kJ/mol, as shown in Figure 9a. Because the diffusion limitation of these two systems is eliminated (previously mentioned), the difference in activation energy implies that these two systems are different with respect to the surface catalysis reaction, which is in agreement with the reported results that the activation energy of oxidation occurring at a gas–solid interface is remarkably different from that at the liquid–solid interface.<sup>8,59–61</sup> In the conventional triphase reactions, the oxidation mainly occurs between alcohol and O<sub>2</sub> dissolved in liquid,<sup>61</sup> whereas in our microbubble system the reaction mainly occurs at the interface between gas, water, and solid, as shown in Figure 9b. The presence of a gas–water–solid interface alters the reaction locus and thus modifies the surface catalysis reaction mechanism, decreasing the reaction activation energy and increasing the reaction rate. This is also supported by the experiments involving smaller bubbles giving rise to higher CE (Figure S13) because the smaller bubbles create a larger reaction interface of gaseous O<sub>2</sub>–liquid–solid and thus decrease the contribution of the reaction between dissolved O<sub>2</sub> and alcohol. Although the underlying reason for the reaction nature change is unclear at present, factors including the interface basicity/acidity, the reactant molecular orientation, and chemical microenvironment<sup>22,28,60,62,63</sup> are quite different from the conventional bulk solution and the reported systems,<sup>8,59–61</sup> which gives the microbubble systems

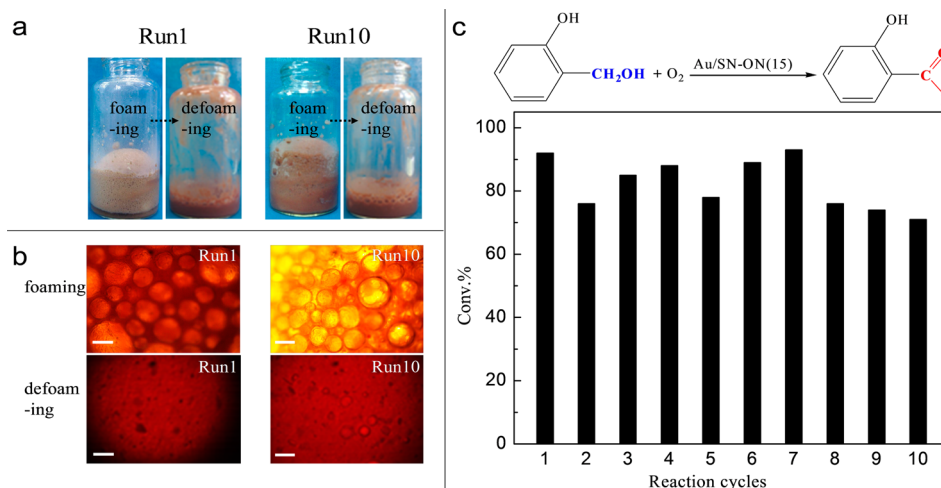


**Figure 8.** (a) Appearance of the 1st and 10th cycles of 2-hydroxybenzyl alcohol oxidation over Au/SN-ON(15) particles before and after the reaction. (b) Corresponding optical micrographs. Scale bar = 200  $\mu\text{m}$ . (c) Conversions in 10 cycles of oxidation of 2-hydroxybenzyl alcohol over Au/SN-ON(15) catalyst particles in the microbubble system. Reaction conditions: 0.1250 g of Au/SN-ON(15) catalyst particles, 0.1875 g of SN-ON(15) particles, 0.25 mmol substrate, 2.5 mL of deionized water, 0.2 MPa, and 900 rpm. The reaction times from the 1st to the 10th reaction cycle are 5, 10, 10, 12, 12, 14, 14, 14, 14, and 14 h, respectively.

**Table 2. Comparison of Alcohol Oxidation in the Microbubble Systems and in the Conventional Bulk Gas–Liquid–Solid Multiphase Systems<sup>a</sup>**

Reactant	Solid <sup>b</sup> /wt.%	S/C <sup>c</sup>	Temp. <sup>d</sup> /°C	P <sup>e</sup> /MPa	t <sup>f</sup> /h	Conv. <sup>g</sup> /%
	12.5	50	80	0.8	9	70 (43)
	12.5	50	50	0.2	5	74 (24)
	12.5	50	80	0.8	8	80 (45)

<sup>a</sup>Reaction conditions: 5 mL of water, 0.5 mmol substrate, 0.25 g of Au/SN-ON(15) catalyst particles, 0.375 g of SN-ON(15) particles, and 900 rpm. For the microbubble systems, before reaction the system was stirred at 1600 rpm (at room temperature) for 10 min to form catalyst particle-stabilized microbubbles. <sup>b</sup>Total mass fraction of catalyst and SN-ON(15) particles with respect to solvent. <sup>c</sup>Molar ratio of substrate (S) to Au catalyst (C). <sup>d</sup>Reaction temperature. <sup>e</sup>O<sub>2</sub> pressure. <sup>f</sup>Reaction time. <sup>g</sup>Conversion determined by GC; the data in parentheses are the conversions obtained in the conventional gas–water–solid three-phase systems.

new potential in tailoring the multiphase reaction process and outcome.

### 3. CONCLUSIONS

A novel strategy that can boost the CE by constructing smart reaction interfaces of gas–water–solid and manifest the gas–water interface catalysis effects is explored. On the basis of surface modification, we have developed a method to prepare pH-responsive inorganic nanoparticles for stabilizing gas microbubbles in water. Their ability to trap and stabilize gas microbubbles can be precisely tuned by varying the modifier composition and also reversibly switched by lowering or raising the pH. As proof of this concept, using such a type of catalyst, the conventional gas–water–solid multiphase systems can be

transformed to a pH-switchable microbubble reaction system, which allows for both high reaction efficiency and easy recycling of the catalyst. The significant reaction efficiency enhancement effect is due to the fact that the microbubble systems create direct contact of gas, water, and solid catalyst phases. Moreover, the microbubble catalysis system results in a lower activation energy for aqueous alcohol oxidation, indicating that the developed microbubble strategy may be a valuable platform to design innovative multiphase catalysis systems.

## 4. EXPERIMENTAL SECTION

**4.1. Preparation of SN-ON(x) Nanoparticles.** As-synthesized silica nanoparticles (1.0 g, dried at 125 °C for 4 h) were dispersed into toluene (5 mL). A mixture of (MeO)<sub>3</sub>SiCH<sub>2</sub>CH<sub>2</sub>CH<sub>2</sub>(NHCH<sub>2</sub>CH<sub>2</sub>)<sub>2</sub>NH<sub>2</sub> and (MeO)<sub>3</sub>Si(CH<sub>2</sub>)<sub>7</sub>CH<sub>3</sub> was added into this suspension. After heating under reflux at 110 °C for 4 h under a N<sub>2</sub> atmosphere, the obtained material was isolated by centrifugation, washed five times with toluene, and dried. The total amount of these two organosilanes was kept at 1.5 mmol, but the molar fraction of triamine silane in this mixture was varied from 5 to 25% (octyl organosilane from 95 to 75%). The modified silica nanoparticles are accordingly denoted as SN-ON(x), where x = 5, 10, 15, 20, and 25.

**4.2. Preparation of Pd/SN-ON(x) and Pd/SN-N.** SN-ON(x) or SN-N (1 g) was added to 5 mL of toluene containing 0.0053 g of Pd(OAc)<sub>2</sub>. After Pd(OAc)<sub>2</sub> was fully absorbed by the particles, the solid material was isolated out through centrifugation. (UV–vis spectroscopy was used to monitor the absorbance of the solution, taking about 4 h.) The Pd-adsorbed solid was further reduced with NaBH<sub>4</sub> dissolved in 5 mL of a mixture of toluene and ethanol (20:1 v/v). After stirring for 4 h at room temperature, the solid was isolated by centrifugation and washed four times with ethanol. After drying under vacuum, the solid catalyst was achieved and is denoted as Au/SN-ON(15) or Pd/SN-ON(x) or Pd/SN-N. The Pd loading for each catalyst was kept at 0.25 wt %, confirmed by ICP-AES determination.



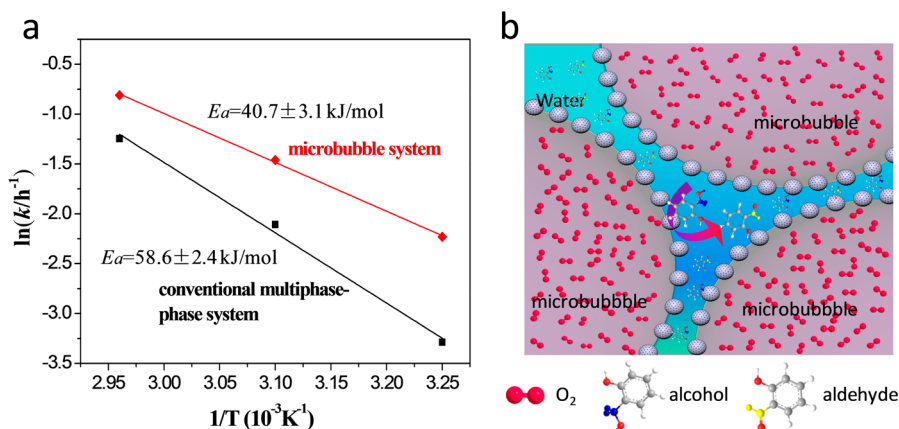


**Figure 9.** (a) Variation of the rate constant for 2-hydroxybenzyl alcohol oxidation with reciprocal temperature in the microbubble system and in the conventional multiphase reaction. (b) Sketch (not to scale) of the microbubble oxidation system.

**4.3. Preparation of Au/SN-ON(15).** SN-ON(15) (1 g) was added to 13.9 mL of  $H AuCl_4$  (2.92 mM) solution. After stirring for 4 h at room temperature,  $H AuCl_4$  was fully absorbed by the particles. (UV-vis spectroscopy was used to monitor the absorbance of the solution.) The solid material was then isolated through centrifugation. The resultant Au-adsorbed solid was reduced with  $NaBH_4$  dissolved in 5 mL of a mixture of toluene and ethanol (20:1 v/v). After stirring for 3 h, the solid was isolated by centrifugation and washed four times with ethanol. After drying under vacuum, the solid catalyst was achieved and is denoted as Au/SN-ON(15).

**4.4. Microbubble Preparation.** SN-ON(*x*) (0.15 g) was added into a glass vessel containing 2 mL of deionized water. Vigorous stirring with a magnetic bar (10 mm in length) at 1200 rpm for 10 min in air led to particle-stabilized foams. The foams stabilized with SN-ON(10), SN-ON(15), and SN-ON(20) particles stood at room temperature for 5 days to monitor their stability. The Au loading on the catalyst is 0.8 wt %.

**4.5. Switching between Microbubble and Microbubble-Free Systems.** A small volume of HCl solution (1 M) was added into the microbubble system stabilized with the SN-ON(15) particles. After stirring gently for 6–8 min, the microbubbles disappeared. A few drops of NaOH solution (1 M) were then added to the above suspension, adjusting the pH of the system to 7–8. After stirring at 1200 rpm for 10 min, microbubbles formed again. After five cycles, the water in the systems was replaced with fresh water to prevent the buildup of salt.

**4.6. Hydrogenation in Microbubble Systems.** A given amount of Pd/SN-ON(*x*) particles and a given amount of SN-ON(*x*) particles were added simultaneously to a 10 mL scaled vial. (The mass ratio of Pd/SN-ON(*x*) to SN-ON(*x*) is given in the footnotes of the corresponding figures and tables.) Reactant and 2.5 mL of deionized water were then added into this vial. The vial was placed in an autoclave (100 mL). After being purged four times with  $H_2$  (99.99%), the  $H_2$  pressure was elevated to the desired pressure. Hydrogenations were conducted under stirring at rate of 1200 rpm (a magnetic stirring bar with length of 10 mm). At the end of reaction, the autoclave was depressurized, and the pH was adjusted to 3–4 using HCl solution. The reaction system was defoamed under gentle stirring. Diethyl ether was used to thoroughly extract organics from water for GC analysis.

**4.7. Oxidation in Microbubble Systems.** Au/SN-ON(15) particles (0.25 g) and 0.375 g of SN-ON(15) particles were added into a 10 mL scaled vial. Substrate (0.5 mmol) and 5 mL of deionized water were then added into this vial. The vial was placed in an autoclave (100 mL). After being purged four times with  $O_2$  (99%), the  $O_2$  atmosphere was elevated to the desired pressure. Oxidations were conducted under stirring at a rate of 1200 rpm (using a magnetic stirring bar with length of 10 mm). After a period of time, the autoclave was depressurized, and the pH was adjusted to 3–4 using HCl solution. The microbubbles in the reaction system were destroyed via gentle stirring.

**4.8. Catalyst Recycling.** At the end of reactions, the autoclave was depressurized, and the pH was adjusted to 3–4 using HCl solution (1 M). The product was thoroughly extracted with diethyl ether. The catalyst dispersed in water was isolated through centrifugation. The obtained catalyst was dispersed in NaOH solution (1 M). After stirring for 10 min, the catalyst was isolated via centrifugation, further washed with methanol, and dried under vacuum. In the next reaction cycle, the recovered catalyst was added into a 10 mL scaled vial. Fresh reactants and deionized water were then added into this vial. The other procedure is the same as that in the first reaction cycle.

**4.9. Characterization.** Samples for transmission electron microscope (TEM) observations were prepared by dispersing the sample powder in ethanol using ultrasound and then allowing a drop of the suspension to evaporate on a copper grid covered with a holey carbon film. TEM images of silica particles were obtained on a JEOL-JEM-2000EX instrument (operated at 120 kV). The electron energy-loss spectroscopy (EELS) and energy dispersive X-ray spectroscopy (EDX) of Pd- or Au-loaded catalysts were achieved on a field-emission transmission electron microscope equipped with an energy dispersive spectrometer (FEI Tecnai G2 F20, 200 kV). Physisorption of  $N_2$  on silica particles was measured by using an ASAP2020 volumetric adsorption analyzer. Before measurement, all samples were outgassed at 120 °C under vacuum for 6 h. The surface area was calculated from the adsorption branch in the relative pressure range of 0.05–0.15 using the Brunauer–Emmett–Teller (BET) equation. Particle-stabilized foams were observed with an optical microscope (XSP-8CA, Shanghai, China). The foam was mounted on a glass slide and was observed with a digital camera. The size distribution of microbubbles was obtained using image analysis software

(Super Image, version 6.0.1.2). Approximately 50 bubbles were randomly selected to determine the size distribution.

C and N contents of functionalized silica particles were determined on a Vario EL instrument (Elementar). X-ray photoelectron spectra (XPS) were recorded on a Kratos Axis Ultra DLD, and the C 1s line at 284.8 eV was used as a reference. Metal contents were determined with an inductively coupled plasma-atomic emission spectrometer (ICP-AES, AtomScan16, TJA Co.). Solid-state NMR spectra were recorded on an Infinityplus 300 MHz spectrometer using the following parameters: for  $^{13}\text{C}$  CP-MAS NMR experiments, 75.4 MHz resonant frequency, 4 kHz spin rate, 4 s pulse delay, 1.0 ms contact time, and hexamethylbenzene as a reference compound; for  $^{13}\text{Si}$  CP-MAS NMR experiments, 79.6 MHz resonant frequency, 4 kHz spin rate, 4.0 s pulse delay, and TMS as a reference compound.

The contact angles of water in air on silica particle disks were measured using a Krüss DSA100 instrument. Before measurement, the powder sample was compressed into a disk with a thickness of approximately 1 mm (ca. 2 MPa). A drop of water (1  $\mu\text{L}$ ) was injected on the sample disk. The appearance of the water drop was recorded at ca. 0.1 s with a digital camera. The contact angle was determined by a photogoniometric method. Zeta potential measurements were conducted using a Brookhaven zeta potential analyzer. A suspension of 2 vol % silica particles was used to determine the surface charge. The pH value of the solution for formulating the suspension was adjusted using  $\text{HNO}_3$  solution (1 M) or  $\text{NaOH}$  solution (1 M) and measured with a pH meter (Shanghai YoKe Instrument Co., Ltd., PHS-3C). Prior to measurements, the suspension was treated with ultrasound for 5 min.

The compositions of the reaction systems were determined with an Agilent7890A gas chromatography (GC) instrument with a flame ionization detector (HP-5 or HP-1 column, 30 m). The conversions were estimated from peak areas.

## ■ ASSOCIATED CONTENT

### Supporting Information

The Supporting Information is available free of charge on the ACS Publications website at DOI: 10.1021/jacs.5b09790.

Experimental details, TEM images, EDX spectrum, water contact angles, zeta potentials, appearance of the particle-stabilized foams, size distribution of the microbubbles in foams, and appearance of foam reaction systems and their optical micrographs. (PDF)

## ■ AUTHOR INFORMATION

### Corresponding Author

\*hgyang@sxu.edu.cn

### Notes

The authors declare no competing financial interest.

## ■ ACKNOWLEDGMENTS

This work is supported by the Natural Science Foundation of China (20903064, 21173137, and 21573136), the Program for New Century Excellent Talents in University (NECT-12-1030), the Program for Middle-aged Innovative Talents of Higher Learning Institutions of Shanxi (20120202), and the Foundation of State Key Laboratory of Coal Conversion (grant no. J15-16-609). The authors thank Ms. Lingling Liu, North University of China, for her help with oxidation experiment.

## ■ REFERENCES

- (1) Minakata, S.; Komatsu, M. *Chem. Rev.* **2009**, *109*, 711.
- (2) Abu-Reziq, R.; Avnir, D.; Blum, J. *Angew. Chem., Int. Ed.* **2002**, *41*, 4132.
- (3) Pera-Titus, M.; Leclercq, L.; Clacens, J.; De Campo, F. D.; Nardello-Rataj, V. *Angew. Chem., Int. Ed.* **2015**, *54*, 2006.
- (4) Liu, S. S.; Sun, K. Q.; Xu, B. Q. *ACS Catal.* **2014**, *4*, 2226.
- (5) Wang, H.; Zhou, W.; Liu, J.-X.; Si, R.; Sun, G.; Zhong, M.-Q.; Su, H.-Y.; Zhao, H.-B.; Rodriguez, J. A.; Pencycook, S. J.; et al. *J. Am. Chem. Soc.* **2013**, *135*, 4149.
- (6) Crossley, S.; Faria, J.; Shen, M.; Resasco, D. E. *Science* **2010**, *327*, 68.
- (7) Mase, N.; Mizumori, T.; Tatemoto, Y. *Chem. Commun.* **2011**, *47*, 2086.
- (8) Lavelle, K.; McMonagle, J. B. *Chem. Eng. Sci.* **2001**, *56*, 5091.
- (9) Liu, H. F.; Zhang, Z. M.; Yang, H. Q.; Cheng, F. Q.; Du, Z. P. *ChemSusChem* **2014**, *7*, 1888.
- (10) Yu, Y. H.; Fu, L. M.; Zhang, F. W.; Zhou, T.; Yang, H. Q. *ChemPhysChem* **2014**, *15*, 841.
- (11) Di Dio, S.; Marchetti, M.; Paganelli, S.; Piccolo, O. *Appl. Catal., A* **2011**, *399*, 205.
- (12) Huang, J. H.; Yang, H. Q. *Chem. Commun.* **2015**, *51*, 7333.
- (13) Hessel, V.; Angeli, P.; Gavrilidis, A.; Löwe, H. *Ind. Eng. Chem. Res.* **2005**, *44*, 9750.
- (14) Kobayashi, J.; Mori, Y.; Okamoto, K.; Akiyama, R.; Ueno, M.; Kitamori, T.; Kobayashi, S. *Science* **2004**, *304*, 1305.
- (15) Dang, T. Y. N.; Gallucci, F.; Van Sint Annaland, M. *Chem. Eng. Sci.* **2014**, *116*, 38.
- (16) Herrmann, U.; Emig, G. *Ind. Eng. Chem. Res.* **1998**, *37*, 759.
- (17) Irfan, M.; Glasnov, T. N.; Kappe, C. O. *ChemSusChem* **2011**, *4*, 300.
- (18) Mase, N.; Isomura, S.; Toda, M.; Watanabe, N. *Synlett* **2013**, *24*, 2225.
- (19) Mase, N.; Mizumori, T. *Piping Engineering* **2011**, *53*, 48.
- (20) Brzozowski, M.; O'Brien, M.; Ley, S. V.; Polyzos, A. *Acc. Chem. Res.* **2015**, *48*, 349.
- (21) Davidovits, P.; Kolb, C. E.; Williams, L. R.; Jayne, J. T.; Worsnop, D. R. *Chem. Rev.* **2006**, *106*, 1323.
- (22) Mishra, H.; Enami, S.; Nielsen, R. J.; Stewart, L. A.; Hoffmann, M. R.; Goddard, W. A., III; Colussi, A. J. *Proc. Natl. Acad. Sci. U. S. A.* **2012**, *109*, 18679.
- (23) Creux, P.; Lachaise, J.; Gracia, A.; Beattie, J. K.; Djerdjev, A. M. *J. Phys. Chem. B* **2009**, *113*, 14146.
- (24) Feng, R. R.; Guo, Y.; Wang, H. F. *J. Chem. Phys.* **2014**, *141*, 18C507-1.
- (25) Bonn, M.; Nagata, Y.; Backus, E. H. G. *Angew. Chem., Int. Ed.* **2015**, *54*, 5560.
- (26) Baer, M. D.; Kuo, I. W.; Tobias, D. J.; Mundy, C. J. *J. Phys. Chem. B* **2014**, *118*, 8364.
- (27) Jorge, M.; Cordeiro, M. N. D. S. *J. Phys. Chem. C* **2007**, *111*, 17612.
- (28) Méndez, A. A.; Voyame, P.; Girault, H. H. *Angew. Chem., Int. Ed.* **2011**, *50*, 7391.
- (29) Tian, C. S.; Ji, N.; Waychunas, G. A.; Shen, Y. R. *J. Am. Chem. Soc.* **2008**, *130*, 13033.
- (30) Du, Z. P.; Bilbao-Montoya, M. P.; Binks, B. P.; Dickinson, E.; Ettelaie, R.; Murray, B. S. *Langmuir* **2003**, *19*, 3106.
- (31) Stocco, A.; Rio, E.; Binks, B. P.; Langevin, D. *Soft Matter* **2011**, *7*, 1260.
- (32) Binks, B. P.; Horozov, T. S. *Angew. Chem., Int. Ed.* **2005**, *44*, 3722.
- (33) Cervantes Martinez, A.; Rio, E.; Delon, G.; Saint-Jalmes, A.; Langevin, D.; Binks, B. P. *Soft Matter* **2008**, *4*, 1531.
- (34) Stocco, A.; Drenckhan, W.; Rio, E.; Langevin, D.; Binks, B. P. *Soft Matter* **2009**, *5*, 2215.
- (35) Binks, B. P.; Murakami, R. *Nat. Mater.* **2006**, *5*, 865.
- (36) Murakami, R.; Moriyama, H.; Yamamoto, M.; Binks, B. P.; Rocher, A. *Adv. Mater.* **2012**, *24*, 767.
- (37) Murakami, R.; Bismarck, A. *Adv. Funct. Mater.* **2010**, *20*, 732.

- (38) Lam, S.; Blanco, E.; Smoukov, S. K.; Velikov, K. P.; Velev, O. D. *J. Am. Chem. Soc.* **2011**, *133*, 13856.
- (39) Dickinson, E.; Ettelaie, R.; Kostakis, T.; Murray, B. S. *Langmuir* **2004**, *20*, 8517.
- (40) Carl, A.; Bannuscher, A.; von Klitzing, R. *Langmuir* **2015**, *31*, 1615.
- (41) Dupin, D.; Howse, J. R.; Armes, S. P.; Randall, D. P. *J. Mater. Chem.* **2008**, *18*, 545.
- (42) Huang, Z. J.; Li, F. B.; Chen, B. F.; Yuan, G. Q. *Green Chem.* **2015**, *17*, 2325.
- (43) Carter, B. O.; Adams, D. J.; Cooper, A. I. *Green Chem.* **2010**, *12*, 783.
- (44) Denkov, N. D. *Langmuir* **2004**, *20*, 9463.
- (45) Karakashev, S. I.; Grozdanova, M. V. *Adv. Colloid Interface Sci.* **2012**, *176–177*, 1.
- (46) Zhang, H.; Miller, C. A.; Garrett, P. R.; Raney, K. H. *J. Colloid Interface Sci.* **2003**, *263*, 633.
- (47) Sha, R. Y.; Meng, Q.; Jiang, L. F. *J. Chem. Technol. Biotechnol.* **2012**, *87*, 368.
- (48) Fujii, S.; Mochizuki, M.; Aono, K.; Hamasaki, S.; Murakami, R.; Nakamura, Y. *Langmuir* **2011**, *27*, 12902.
- (49) Yang, H. Q.; Zhou, T. W.; Zhang, J. *Angew. Chem., Int. Ed.* **2013**, *52*, 7455.
- (50) Binks, B. P. *Curr. Opin. Colloid Interface Sci.* **2002**, *7*, 21.
- (51) Binks, B. P.; Murakami, R.; Armes, S. P.; Fujii, S.; Schmid, A. *Langmuir* **2007**, *23*, 8691.
- (52) Joó, F. *Acc. Chem. Res.* **2002**, *35*, 738.
- (53) Anderson, J. A.; Athawale, A.; Imrie, F. E.; McKenna, F.-M.; McCue, A.; Molyneux, D.; Power, K.; Shand, M.; Wells, R. P. K. *J. Catal.* **2010**, *270*, 9.
- (54) Li, X. H.; Zheng, W. L.; Pan, H. Y.; Chen, L.; Yu, Y.; Wu, P. J. *Catal.* **2013**, *300*, 9.
- (55) Tsunoyama, H.; Sakurai, H.; Negishi, Y.; Tsukuda, T. *J. Am. Chem. Soc.* **2005**, *127*, 9374.
- (56) Shang, C.; Liu, Z. P. *J. Am. Chem. Soc.* **2011**, *133*, 9938.
- (57) Casanova, O.; Iborra, S.; Corma, A. *ChemSusChem* **2009**, *2*, 1138.
- (58) Hou, W. B.; Dehm, N. A.; Scott, R. W. J. *J. Catal.* **2008**, *253*, 22.
- (59) Wang, H.; An, K.; Sapi, A.; Liu, F.; Somorjai, G. A. *Catal. Lett.* **2014**, *144*, 1930.
- (60) Wang, H.; Sapi, A.; Thompson, C. M.; Liu, F.; Zhrebetsky, D.; Krier, J. M.; Carl, L. M.; Cai, X.; Wang, L. W.; Somorjai, G. A. *J. Am. Chem. Soc.* **2014**, *136*, 10515.
- (61) Lavelle, K.; McMonagle, J. B. *Chem. Eng. Sci.* **2001**, *56*, 5091.
- (62) Mundy, C. J.; Kuo, I-F. W.; Tuckerman, M. E.; Lee, H.; Tobias, D. J. *Chem. Phys. Lett.* **2009**, *481*, 2.
- (63) Marinova, K. G.; Alargova, R. G.; Denkov, N. D.; Velev, O. D.; Petsev, D. N.; Ivanov, I. B.; Borwankar, R. P. *Langmuir* **1996**, *12*, 2045.